ACS APPLIED ENERGY MATERIALS

www.acsaem.org Article

Hydrogen-Rich Gas Production by Steam Reforming and Oxidative Steam Reforming of Methanol over $La_{0.6}Sr_{0.4}CoO_{3-\delta}$: Effects of Preparation, Operation Conditions, and Redox Cycles

Miguel Morales,* Miguel Ángel Laguna-Bercero, and Emilio Jiménez-Piqué

Cite This: ACS Appl. Energy Mater. 2023, 6, 7887−7898 Read Online

ACCESS | Metrics & More | Article Recommendations

ABSTRACT: $La_{0.6}Sr_{0.4}CoO_{3-\delta}$ (LSC) perovskite, as a potential catalyst precursor for hydrogen (H_2)-rich production by steam reforming of methanol (SRM) and oxidative steam reforming of methanol (OSRM), was investigated. For this purpose, LSC was synthesized by the citrate sol−gel method and characterized by complementary analytical techniques. The catalytic activity was studied for the as-prepared and prereduced LSC and compared with the undoped $LaCoO_{3-\delta}$ (LCO) at several feed gas compositions. Furthermore, the degradation and regeneration of LSC under repeated redox cycles were studied. The results evidenced that the increase in the water/methanol ratio under SRM, and the O_2 addition under OSRM, increased the CO_2 formation and decreased both the H_2 selectivity and catalyst deactivation caused by carbon deposition. Methanol conversion of the prereduced LSC was significantly enhanced at a lower temperature than that of as-prepared LSC and undoped LCO. This was attributed to the performance of metallic cobalt nanoparticles highly dispersed under reducing atmospheres. The reoxidation program in repetitive redox cycles played a crucial role in the regeneration of catalysts, which could be regenerated to the initial perovskite structure under a specific thermal treatment, minimizing the degradation of the catalytic activity and surface.

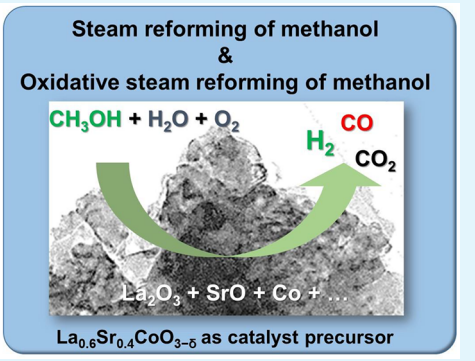

KEYWORDS: *methanol, hydrogen production, steam reforming, nanoparticles, perovskite, solid oxide fuel cells*

1. INTRODUCTION

Catalytic steam reforming of methanol (SRM) presents a great potential to supply hydrogen (H_2) for fuel cells.[1] Although methanol (CH_3OH) is highly toxic and miscible in water, it possesses several advantages, such as a high hydrogen-to-carbon ratio, liquid state at atmospheric conditions, and biodegradability.[2] Compared to other fuels like hydrogen, synthesis gas, or methane, the hydrogen volumetric density in methanol is higher than those of either compressed fuel gas or liquid H_2. It is easier to distribute with the existing infrastructure and safer to handle than compressed H_2.[3,4] Like other fuels, methanol can be a carbon-neutral renewable feedstock because it is easily obtained as a synthetic fuel from renewable sources.[5,6] On the other hand, the operating temperatures for SRM (200−300 °C) are lower compared to other reforming processes such as ethanol steam reforming around 400 °C[7,8] or methane steam reforming above 500 °C.[9] The SRM process is mainly described by three main reactions: direct SRM (eq 1), methanol decomposition (MD) (eq 2), and reverse water−gas shift (RWGS) (eq 3).[10,11]

$$CH_3OH + H_2O \rightleftharpoons CO_2 + 3H_2 \qquad \Delta H^\circ = 50\ \text{kJ mol}^{-1} \tag{1}$$

$$CH_3OH \rightleftharpoons CO + 2H_2 \qquad \Delta H^\circ = 91\ \text{kJ mol}^{-1} \tag{2}$$

$$CO_2 + H_2 \rightleftharpoons CO + H_2O \qquad \Delta H^\circ = 41\ \text{kJ mol}^{-1} \tag{3}$$

MD (eq 2) and RWGS (eq 3) occur simultaneously with SRM. Because the overall process is remarkably endothermic, it consumes so much energy that it has to be supplied from an external source. The addition of O_2 to the SRM process is a common practice to combine the steam reforming and partial oxidation reactions that could approximate an autothermal oxidative steam reforming of methanol (OSRM; eq 4):

$$CH_3OH + (1 - 2a)H_2O + aO_2 \rightleftharpoons (3 - 2a)H_2 + CO_2 \qquad (0 \le a \le 0.5) \tag{4}$$

Autothermal SRM can be reached at around $a = 0.1$−0.2.[12] Higher O_2 compositions favor the formation of CO_2 and H_2O,

Received: March 28, 2023
Accepted: July 10, 2023
Published: July 25, 2023

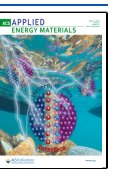

as well as a strongly exothermic process, because partial oxidation becomes predominant.

Typically, the use of SRM includes the production of H_2 for proton exchange membrane fuel cells (PEMFCs). However, the formation of CO, as a byproduct of reforming, is one of the drawbacks of SRM because CO concentrations above 10 ppm lead to catalyst poisoning of the PEMFC anode.[1] Thus, the catalyst used in the SRM process must possess high catalytic activity at low temperatures, minimization of CO production, high hydrogen selectivity, and high stability. SRM may be effectively carried out over the commercially available catalyst based on either Cu or Pd supported typically on ZnO and Al_2O_3.[13] Pd-based catalysts exhibit better thermal stability than Cu-based ones with a CO_2 selectivity close to 100%.[14,15] The optimal operating conditions of Cu/Zn/Al catalysts, mainly used in small hydrogen plants, are close to the H_2O/CH_3OH ratio of 1.3 and a temperature range of 250−300 °C.[16]

Alternatively, perovskite-type oxides, with the general formula $ABO_{3\pm\delta}$, where A represents rare earths (e.g., La) or alkali/alkaline-earth (e.g., Ca, Sr) metal cations and B depicts transition-metal cations (e.g., Co, Cu, and Fe), are promising highly active catalyst precursors to produce H_2 from different reforming reactions of alcohols and hydrocarbons.[17,18] Thus, their catalytic properties can be tailored for specific applications by partially substituting A and/or B site cations with suitable ones while preserving the perovskite crystal structure. Lanthanum cobaltite perovskites have been implemented as catalyst precursors for many oxidation and reduction reactions in heterogeneous catalysis.[18] Among others, Cu- and Pd-doped perovskites of the $LaCoO_3$ type $LaCo_{1-x-y}M_xM_yO_{3\pm\delta}$ (M = Cu, Pd, Zn) are especially interesting for SMR because the presence of Cu and Pd in the $LaCoO_3$ structure increases O-ion mobility and enhances the catalytic activity of SMR. For instance, $LaCo_{0.7}Cu_{0.3}O_{3-\delta}$,[19] $LaCo_{1-x-y}Pd_xZn_yO_{3\pm\delta}$,[20,21] $La_2CuO_4/CuO/ZnO/Al_2O_3$,[22] $CuO/La_{1-x}Ce_xCrO_3$,[23] and $SrCo_{1-x}Cu_xO_{3\pm\delta}$[24] are good candidates for the SRM process because their metal oxides generated in reducing atmospheres can stabilize Cu and/or Pd, avoiding migration and sintering of particles. Nevertheless, these perovskite-type oxides perform poorly at relatively low temperatures compared to Cu or Pd supported on ZnO/Al_2O_3 because CH_3OH conversion starts above 250−300 °C and the CO_2 selectivity is between 50% and 70%. In this regard, these mixtures of H_2 and CO, named synthesis gas (syngas), can be attractive for feeding solid oxide fuel cells (SOFCs).[25] Compared to PEMFCs, SOFCs are much more flexible because they can effectively use different mixtures of H_2, CO, and other gases as fuels. Therefore, lanthanum cobaltite perovskites may present a high potential use for SRM to supply SOFC applications, but unfortunately literature is very scarce. To the best of the authors' knowledge, only $LaCo_{0.7}Cu_{0.3}O_{3-\delta}$,[19] $LaCo_{1-x-y}Pd_xZn_yO_{3\pm\delta}$,[20] and $La_{0.6}Sr_{0.4}Co_{1-y}Fe_yO_{3-\delta}$[26] have reported high CH_3OH conversions and H_2 and CO_2 selectivities of about 80−90% and 40−70%, respectively. The SRM performance significantly depended on the catalyst composition, enhanced by increasing Co/Fe ratio.[20] The partial substitution of Co with both Pd and Zn considerably suppressed the decomposition reaction, thus increasing the CO_2 selectivity.[26] In addition, the SRM activity was also affected by the H_2O/CH_3OH ratio, yielding better CH_3OH conversion and CO_2 selectivity with excess H_2O in the feed.[20] The reaction mixture obtained higher catalytic activity when O_2 was added.[19]

Given the works above, Sr-substituted lanthanum−cobalt oxides ($La_{1-x}Sr_xCoO_{3-\delta}$) may be another interesting perovskite-type oxide for SRM and OSRM, particularly when a high H_2/CO ratio is not required. Then, the absence of Pd in the catalysts could be an advantage in decreasing their price. Furthermore, the strontium oxide in $LaXCoO_3$ (X = Mg, Ca, Sr, Ce) could enhance the activity and stability, such as for steam reforming of ethanol, showing a better catalytic performance than the other compositions.[27] In this regard, $La_{1-x}Sr_xCoO_3$ is known to be interesting because of its excellent performance for multiple catalytic applications: oxidation of CO, propane, and methane[28,29] soot oxidation activity,[30] toluene combustion,[31] Li−O_2 battery,[32] and solar photocatalyst.[33] Furthermore, $La_{1-x}Sr_xCoO_{3-\delta}$ (x = 0.2−0.5) is typically used, showing excellent performances as an oxygen electrode and a current collector for SOFCs[34−36] and solid oxide electrolyzer cells (SOECs)[37−39] and also as a cathode for single-chamber SOFCs.[40,41] Among the studied compositions of $La_{1-x}Sr_xCoO_{3-\delta}$ for catalytic applications, $La_{0.6}Sr_{0.4}CoO_{3-\delta}$ (LSC) showed the best catalytic activity, attributed to the highest oxygen chemisorption and desorption capacity.[28−30] In this regard, Morales et al.[42−44] reported the performance and stability of $La_{1-x}Sr_xCoO_{3-\delta}$ (x = 0.4 and 0.5) perovskites, as a catalyst precursor, for the production of H_2 and syngas by the partial oxidation of methane and steam reforming of ethanol. The results evidenced a remarkable catalytic activity due to the stability of Co particles, which were highly dispersed in their reduced state. Similarly, Chen et al.[45] recently reported a series of A-site Sr-doped $La_{1-x}Sr_xCeO_{3-\delta}$ (x = 0.2, 0.4, 0.6, 0.8) perovskite catalysts for H_2 production by SRM, showing that $La_{0.6}Sr_{0.4}CeO_{3-\delta}$ exhibited the best performance at optimal reaction conditions. In summary, Sr-substituted lanthanum−cobalt oxide perovskites may be potential catalytic precursors for the SRM and OSRM processes to supply H_2-rich gas for SOFC applications. However, few studies reported the SRM and OSRM over LSC perovskites, and information on how the preparation, operation conditions, and degradation under redox cycles affected the catalytic activity is still scarce. Meanwhile, these issues also have a great interest in the SOFC development using LSC perovskites because their degradation is primarily due to Sr segregation on the electrode surfaces at operating temperatures higher than 500 °C.[46,47] Recently, several strategies to control Sr segregation have been reported on the modification of surfaces with more and less reducible cations, the control and change of the oxygen partial pressure and applied voltage, the substitution of isovalent A- or B-site cations with different ionic radii, or the lowering of the operating temperature to deactivate Sr segregation thermodynamically and kinetically, among others.[48−50] Despite many efforts, completely effective practical solutions have not yet been proposed to inhibit Sr segregation, and, therefore, the use of thermal treatments and HCl etching to remove the Sr-rich particles at the surface of the used LSC have been proposed.[50]

Here, we propose to study the LSC under multiple SRM and OSRM conditions because understanding the preparation, operation conditions, and redox cycles of SRM and OSRM perovskites is critical for finding new strategies, optimizing their performance, and enabling their practical application in catalysis but also in other systems such as SOECs for renewable energy conversion and storage. In the present work, LSC was studied as a precursor catalyst for SRM and OSRM. For this purpose, LSC was synthesized by the sol−gel citrate method. The prepared material was deeply charac-

https://doi.org/10.1021/acsaem.3c00778
ACS Appl. Energy Mater. 2023, 6, 7887−7898

terized by different complementary analysis techniques, and, subsequently, the catalytic activity toward SRM and OSRM was investigated. Particular attention was paid to studying the effect of LSC's reductive thermal pretreatment and feed gas composition on the catalytic performance. Furthermore, the degradation and regeneration of LSC under several reaction conditions and repeated redox cycles were investigated.

2. EXPERIMENTAL PROCEDURE

2.1. Catalyst Preparation. $La_{0.6}Sr_{0.4}CoO_{3-\delta}$ (LSC) perovskite was synthesized by the sol−gel citrate method. The detailed synthesis procedure was described elsewhere.[42] Metal precursors $La(NO_3)_3 \cdot 6H_2O$ (Alfa Aesar, 99.9%), $Sr(NO_3)_2$ (Alfa Aesar, 99.9%), and $Co(NO_3)_2 \cdot 6H_2O$ (Alfa Aesar, 99.9%) were weighed in stoichiometric amounts and dissolved in deionized water. Subsequently, citric acid and ethylenediaminetetraacetic acid were added to the metal ion solution. The aqueous solution was slowly evaporated under stirring at 75 °C until a gel was obtained. The resulting gel was dried at 110 °C, homogenized in an agate mortar, and calcined at 500 °C to promote decomposition of the organic fraction. Finally, the precursor was calcined at 900 °C in synthetic air for 12 h and at 300 °C in pure O_2 for 72 h.

2.2. Catalyst Characterization. The catalyst was characterized in different oxidation states: as-prepared LSC, after a reductive thermal treatment in 5% H_2/Ar at 650 °C for 1 h, after SRM and OSRM tests, and after a specific thermal treatment of regeneration. To investigate *in situ* regeneration of the LSC precursor under the reaction conditions, redox cyclic tests were carried out, reoxidizing the catalyst by decreasing the temperature from reaction temperature (600 °C) to room temperature (RT) in several cooling programs: a quenching in N_2, a quenching under SRM and OSRM, and a slow cooling under SRM, OSRM, and air. Regeneration experiments of the LSC precursor were also carried out under synthetic air at 900 °C for 12 h and subsequently at 300 °C for 72 h, similar to that described previously.[43,44]

The specific surface area of the catalysts was determined by the Brunauer−Emmett−Teller method using a Micromeritics model Tristar 3000, measuring the nitrogen adsorption at 77 K. Temperature-programmed reduction (TPR) experiments were performed in a reactor equipped with a thermal conductivity detector (TCD). A gas mixture of 5% H_2/Ar (30 mL min^{-1}) was used to reduce 50 mg of LSC by heating from 100 to 800 °C at 10 °C min^{-1}. Phase analysis of the synthesized and thermally treated powders was performed by X-ray diffraction (XRD). The XRD patterns were obtained by using a Siemens 2000 diffractometer with Cu Kα radiation (40 kV, 40 mA, λ = 0.154 nm). The XRD patterns were collected in the range 2θ = 20−80°, and the crystalline phases were identified using the JCPDS database. The crystallite sizes were estimated through the line broadening of the XRD peaks using the Scherrer equation.[51] The surface properties related to the chemical states and surface compositions of La, Sr, Co, and O in the LSC samples were determined by X-ray photoelectron spectroscopy (XPS). XPS analyses were conducted in an ultrahigh-vacuum multichamber system by SPECS with a PHOIBOS 150 EP hemispherical energy analyzer and an MCD-9 detector XR-50. It possesses an X-ray source with a twin anode (Al and Mg) and a high-pressure and high-temperature chamber for gas treatments of the samples. The samples were compensated for charging with a low-energy electron beam, and the peak of C 1s (binding energy = 284.4 eV) was used to correct for sample charging effects.[52] *SpecsLab Prodigy*, an experiment control software package, was used for data acquisition and *CasaXPS* for spectral analysis. The catalyst microstructures were observed by transmission electron microscopy (TEM; Titan G2 60-300, USA) and scanning electron microscopy (SEM; Carl Zeiss Merlin, Germany) equipped with energy-dispersive spectroscopy (EDS; Oxford Instruments INCA-350 system, United Kingdom). The samples were coated with carbon to minimize the electrical charge on the surface.

2.3. Catalytic Tests. SRM and OSRM experiments were carried out in a fixed-bed quartz tubular reactor (5 mm inner diameter) at atmospheric pressure. The catalytic tests were performed using 50 mg of LSC packed on a bed of quartz wool in the reactor. The reactor was kept in a horizontal tubular furnace. Two K-type thermocouples were used: one outside the reactor to control the furnace temperature using a Eurotherm PID controller and another in contact with the catalyst to measure the bed temperature. Before catalyst tests, several blanks (without catalyst) were analyzed to confirm the reactor's absence of direct oxidation reactions. Before the SRM reaction, the catalyst precursor was reduced at 650 °C for 1 h in 5 vol % H_2/Ar (30 mL min^{-1}) and then cooled under N_2 (30 mL min^{-1}) to the initial testing temperature of 150 °C. In addition, several tests were performed with the as-prepared catalyst (without reductive pretreatment) to study the effect of the previous oxidation state of the catalyst on the catalytic activity. Afterward, the reaction mixture was introduced to the reactor to analyze the impact of the temperature, varying the feed composition of the $O_2/H_2O/CH_3OH$ molar ratio on the methanol conversion. Finally, the selectivities of the products were investigated under different SRM and OSRM conditions.

For SRM tests, a mixture of vaporized water−methanol, with H_2O/CH_3OH molar ratios of 1.3:1, 2:1, and 4:1, and N_2 carrier gas was cofed to the reactor using a mass flow controller (Bronkhorst High-Tech). The reaction gas mixture was composed of 80 vol % N_2 and 20 vol % (CH_3OH + H_2O). The water−methanol solution was continuously dosed by a peristaltic pump. The gas hourly space velocity resulting from the total gas mixture was 40000 h^{-1}. For OSRM tests, O_2 was added to the reaction mixture SRM, using a mass flow controller (Bronkhorst High-Tech), with $O_2/H_2O/CH_3OH$ molar ratios of 0.1:1.3:1, 0.2:1.3:1, and 0.3:1.3:1. The other conditions were similar to those of SRM. The effluent gases were analyzed by online gas chromatography (3000A micro GC, Agilent Technologies, USA) equipped with three channels, using a molecular sieve, a Poraplot, QV-1 columns, and a TCD. The chromatograph was calibrated using known flow rates of pure gases (CO, CO_2, and H_2) with N_2 as the internal standard. Other byproducts, such as methanol or ethylene, were not detected significantly. Methanol conversion and selectivity to products were determined as follows:

$$X_{CH_3OH}\ (\%) = \frac{n(CO)_{out} + n(CO_2)_{out}}{n(CH_3OH)_{in}} \times 100$$

$$H_2\ \text{selectivity}\ (\%) = \frac{n(H_2)}{3[n(CO) + n(CO_2)]} \times 100$$

$$CO_2\ \text{selectivity}\ (\%) = \frac{n(CO_2)}{n(CO) + n(CO_2)} \times 100$$

where $n(CH_3OH)_{in}$ is the flow rate (mol min^{-1}) at the reactor inlet and $n(CO)_{out}$, $n(CO_2)_{out}$, and $n(H_2)_{out}$ are the flow rates (mol min^{-1}) of CO, CO_2, and H_2, respectively, at the reactor outlet.

3. RESULTS AND DISCUSSION

3.1. Catalyst Characterization. Figure 1 shows the TPR results of LSC and $LaCoO_{3-\delta}$ (LCO). Co reduction in both catalyst precursors occurred in two steps. In the case of LCO, the initial reduction of Co^{3+} to Co^{2+} resulted between 300 and 420 °C with a peak centered at ∼380 °C, and the complete reduction of Co^{2+} to Co^0 occurred at temperatures of 440−660 °C (maximum at ∼570 °C). Similar to the LCO perovskite, the Co of LSC was first reduced between 200 and 400 °C due to a one-electron reaction, which took place with two peaks at ∼280 and ∼380 °C. The second reduction step was a two-electron process in the 430−680 °C range, with two maxima centered at ∼440 and ∼640 °C. Compared to LCO, the TPR peaks of LSC were shifted toward lower temperatures. The Sr^{2+} doping in LSC led to a less stable structure, increasing the average oxidation state of Co^{3+} to Co^{4+} and/or the generation of oxygen vacancies.[53,54] These TPR data suggested that the presence of Sr^{2+} in LCO-based perovskites should promote the

https://doi.org/10.1021/acsaem.3c00778
ACS Appl. Energy Mater. 2023, 6, 7887−7898

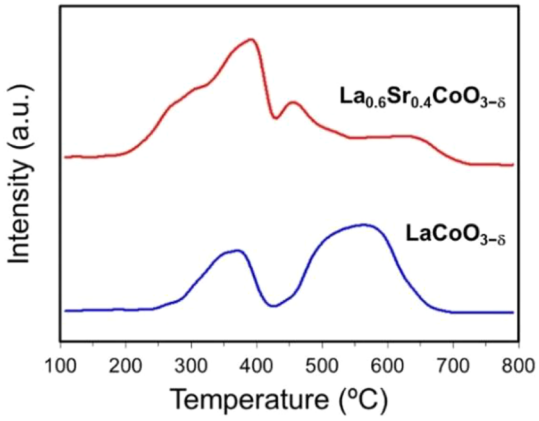

Figure 1. H_2-TPR curves of the LSC and LCO perovskites.

reduction process and, consequently, the SRM of LSC at temperatures lower than those of LCO.

Figure 2 shows the XRD patterns and SEM images of LSC as-prepared and after a reductive thermal treatment at 650 °C

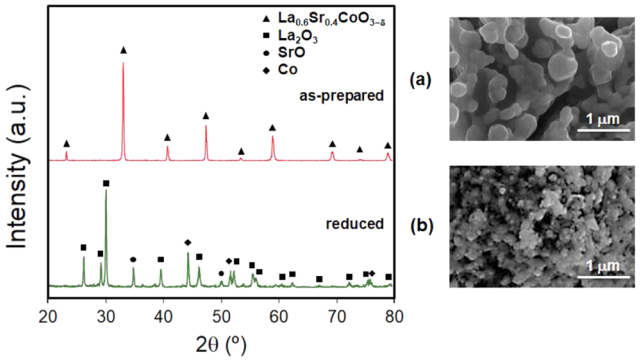

Figure 2. XRD patterns for LSC: (a) as-prepared and (b) after reduction in 5% H_2/Ar at 650 °C for 1 h. Phases identified from JCPDS cards: cubic $La_{0.6}Sr_{0.4}CoO_{3-\delta}$ (JCPDS 48-0121), hexagonal La_2O_3 (JCPDS 05-0602), cubic SrO (JCPDS 48-1477), and cubic Co (JCPDS 15-0806).

for 1 h in 5 vol % H_2/Ar. XRD analysis evidenced that as-prepared LSC presents the cubic perovskite structure, the only phase with a highly crystalline symmetry. After the reductive thermal treatment, XRD exhibited the formation of a mixture of phases composed of cubic Co, hexagonal La_2O_3, and cubic SrO. Therefore, due to the reduction reaction, the total decomposition of LSC generated the following process: $La_{0.6}Sr_{0.4}CoO_{3-\delta} \rightarrow Co/La_2O_3/SrO$. These results were in good agreement with the TPR data. The crystallite sizes were about 20−30 nm, as determined from the XRD data using Scherrer's formula. This suggested that Co nanoparticles were highly dispersed on a La_2O_3 and SrO particles matrix. SEM and TEM micrographs of LSC showed that much larger particle dispersion and smaller particle size were achieved in the reduced state (Figures 2 and 3). The specific surface areas of the precursor increased from 6 $m^2\ g^{-1}$ (as-prepared) to 56 $m^2\ g^{-1}$ after the reduction process, which is in good agreement with the TEM images and XRD patterns. This strong increase in the specific surface area of the reduced precursor is expected due to the calcination conditions at temperatures as high as 900 °C to form the perovskite phase and the capacity of perovskite-type oxides for yielding an excellent metallic

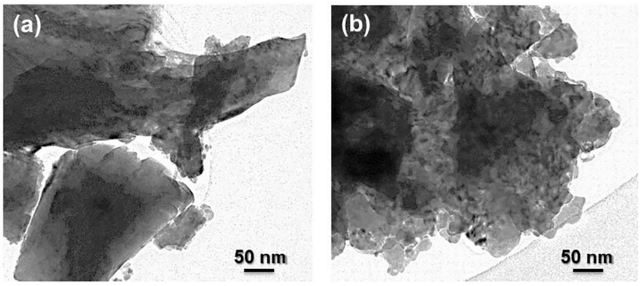

Figure 3. TEM images for LSC: (a) as-prepared and (b) after reduction in 5% H_2/Ar at 650 °C for 1 h.

dispersion formed by one or several metals in a matrix of metal oxides.[18,55]

Figure 4 shows the XPS spectra of La 3d, Sr 3d, Co 2p, and O 1s corresponding to as-prepared LSC and after the reduction of LSC, which were obtained in an ultrahigh-vacuum chamber. Additionally, surface compositions of the samples derived from XPS measurements are listed in Table 1. The La 3d level was characterized by a double peak for each spin−orbit component (Figure 4a). The positions and shapes of the La 3d peaks for both samples were similar to those reported in the literature for LSC.[30,56] In the La 3d signal, the double contribution of each spin−orbit is characteristic of La^{3+} and so is a fingerprint of the oxidation state. The samples exhibited different splittings (around 0.4 eV) in the La XPS peaks, 3.5 and 4.0 eV for the as-prepared and reduced samples, respectively. This is related to the chemical states present in each sample because the strong electron orbital−spin angular momentum interactions cause a splitting of the La XPS peaks. In the as-prepared sample, the splitting is close to that of $La_2(CO)_3$, in concordance with the Sr XPS results. After reduction, the splitting increased toward the value for lanthanum oxide, indicating that the carbonate amount decreased, but it is not pure lanthanum oxide bonding. The results are consistent with a mixture of La_2O_3, $La_2(CO)_3$, and $La(OH)_3$. Figure 4b exhibits the Sr $3d_{5/2}$ region (~132 eV) characteristic of Sr^{2+} in the perovskite phase (LSC lattice). In addition, the Sr $3d_{3/2}$ peak (~133−134 eV) indicates the formation of $SrCO_3$[56] (~133 eV), and the contribution at higher binding energy (~134 eV) suggested the presence of SrO.[26] The Sr 3d spectral comparison for the as-prepared and reduced LSC evidenced the significant intensity of the Sr 3d peak in $SrCO_3$ after LSC reduction, which was associated with the Sr tendency to interact with the atmospheric CO_2.[56] For the as-prepared LSC in Figure 4c, the high intensities of Co $2p_{1/2}$ and Co $2p_{3/2}$ at binding energies of ~779 and ~783 eV and ~794 and ~795 eV, respectively, indicated that the Co was mainly in the states of Co^{3+}/Co^{4+} and Co^{2+}, respectively.[57,58] As observed by other researchers for LSC,[59] we note that Co^{3+} and Co^{4+} were indistinguishable and could not be quantified from the main peaks of the Co 2p XPS spectra, while both states are expected to exist on/in LSC at high temperatures. After the reduction treatment, both Co 2p peaks were wider than the as-prepared LSC due to the significant presence of metallic Co at ~778 and ~793 eV, respectively, and the decrease of the Co^{3+}/Co^{4+} peak. In addition, the surface amount of Co after the reduction catalyst became higher than that of the as-prepared one, evidencing that the Co species got out on the surface. Figure 4d shows the O 1s region with four peaks at ~528, ~529, ~531−532, and

https://doi.org/10.1021/acsaem.3c00778
ACS Appl. Energy Mater. 2023, 6, 7887−7898

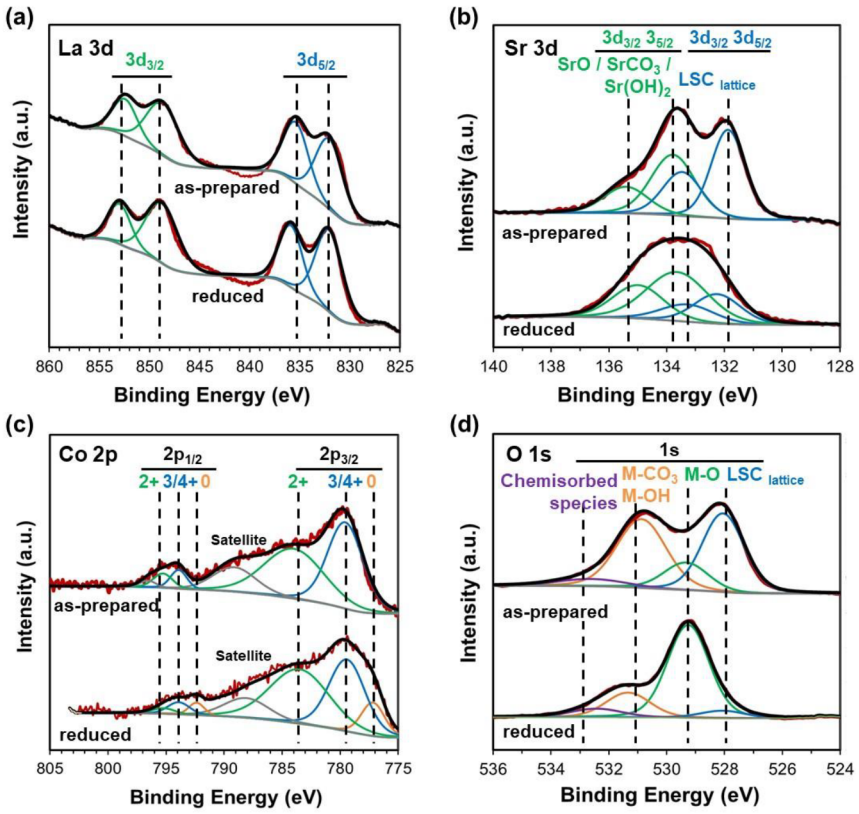

Figure 4. XPS spectra of (a) La 3d, (b) Sr 3d, (c) Co 2p, and (d) O 1s corresponding to LSC as-prepared and after the reduction process.

Table 1. Nominal and XPS Compositions of LSC As-prepared and after the Reduction Process

		La	Sr	Co	O
Nominal (atomic %)		10	7	17	66
XPS (atomic %)	As-prepared	11	10	16	64
	After reduction	17	18	20	45

~533 eV attributed to lattice O in the perovskite, M−O (M = La, Co, Sr) in pure oxides, hydroxyl groups (~531 eV), and carbonates species (~532 eV), and chemisorbed water or O-containing species, respectively.[33,46,60] After the reduction, the O 1s atom within the binding energy range of the LSC lattice was strongly decreased, suggesting a loss of O content at the surface of the reduced catalyst. An O loss at the surface of the reduced precursor was quantified from deconvolution of the fitted spectrum curves (Table 1). In addition, a certain segregation of the A site cation, especially in Sr, on the surface was observed in as-prepared and reduced precursors, which is in good agreement with previous works.[33,46,61]

The characterization results suggest that a reductive pretreatment of LSC in 5 vol % H_2/Ar at 650 °C for 1 h was beneficial to achieving highly dispersed metallic Co nanoparticles on a metal oxide matrix. Consequently, it was proposed to start the catalytic tests under SRM and OSRM with a totally reduced LSC catalyst precursor.

3.2. Catalytic Performance. *3.2.1. Effect of the Oxidation State of the Catalyst.* Because the catalytic properties depend on the initial oxidation state of the catalyst, the effect of reductive thermal pretreatment of the catalyst precursor on the CH_3OH conversion and product selectivity was investigated. Figure 5 shows the CH_3OH conversion and CO_2 and H_2 selectivity under the SRM reaction, for an as-prepared LSC and after a reductive pretreatment in 5 vol % H_2/Ar at 650 °C for 1 h. In addition, the catalytic properties obtained for an as-prepared LCO were also reported for comparison with the as-prepared LSC. As shown in Figure 5a, the significant CH_3OH conversion of as-prepared LSC started at ~300 °C and gradually enhanced with an increase of the temperature, and complete conversion was reached around 400 °C. In contrast, the catalytic activity of LSC after a reductive pretreatment at 650 °C remarkably enhanced at a lower temperature, as the CH_3OH conversion started around 250 °C, and the total conversion was completed at ~350 °C. In the temperature range of 275−425 °C, the CO_2 and H_2 selectivity progressively increased to about 65% and 90%, respectively (Figure 5b). Above 425 °C, the selectivity of CO_2 and H_2 dropped with an increase in the temperature, exhibiting a similar tendency for both as-prepared and pretreated LSC. These results confirmed that the previous state of the catalyst governed the catalytic activity at low temperature. The low CO_2 and H_2 selectivity values at low temperatures indicated the importance of the MD reaction, which decreased with an increase in the temperature to reach a maximum value at ~425 °C. Above ~425 °C, RWGS contributed to diminishing the CO_2 and H_2 selectivity, evidencing the critical role of thermodynamics in the SRM reaction over this catalyst. At this point, as reported in previous works,[18] surface segregation of Co as Co^0 induced by the reductive environmental conditions is a fundamental step for active species activation. The role of reductive thermal pretreatment of the catalyst precursor on the activation of active species at the microscopic level will be discussed in the next section on catalyst characterization under SRM and OSRM.

https://doi.org/10.1021/acsaem.3c00778
ACS Appl. Energy Mater. 2023, 6, 7887−7898

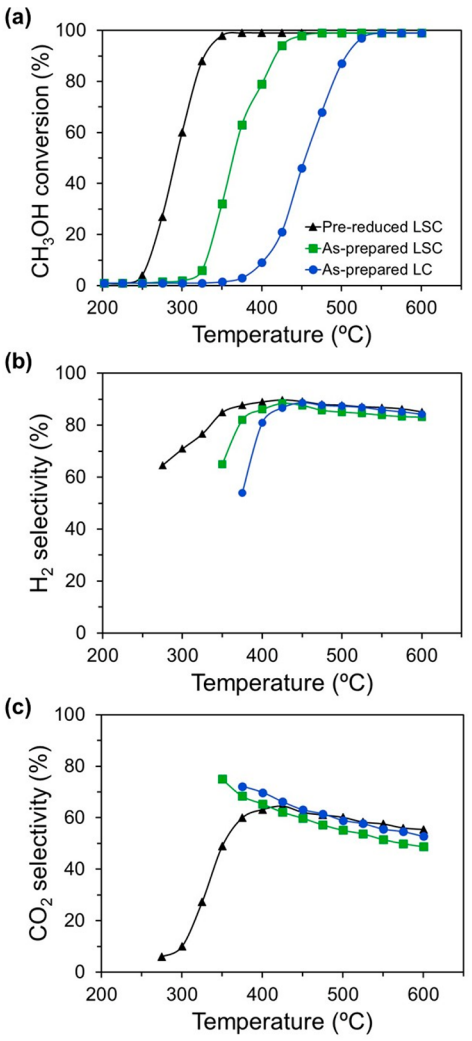

Figure 5. Effect of reductive thermal pretreatment in LSC on (a) CH_3OH conversion, (b) H_2 selectivity, and (c) CO_2 selectivity at a H_2O/CH_3OH ratio of 1.3. The catalytic properties obtained for as-prepared LCO are reported for a comparison with those of as-prepared LSC.

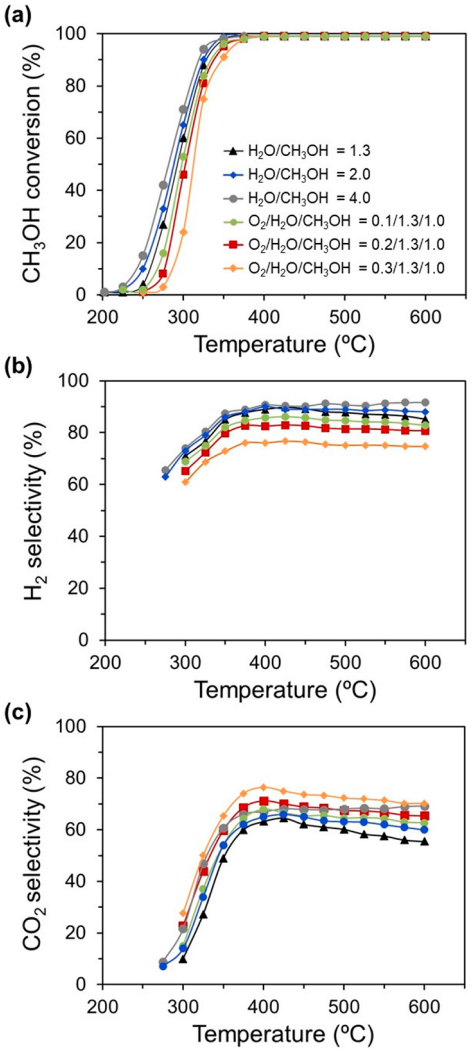

Figure 6. Effect of the feed composition on the (a) CH_3OH conversion, (b) H_2 selectivity, and (c) CO_2 selectivity after a reductive pretreatment at 600 °C of LSC.

On the other hand, the Sr influence on the SRM performance of LSC was compared to that of undoped LCO. As shown in Figure 5a, the CH_3OH conversion of as-prepared LCO started above ~350 °C, and the total conversion was completed at ~550 °C. Thus, the partial substitution of La by Sr reduced the temperature at which the catalyst started the SRM. These results were in good agreement with the TPR experiments, in which the TPR peaks of LSC were shifted toward lower temperatures concerning those of LCO. The values and trends of the CO_2 and H_2 selectivity for both LCO and LSC were close because the active phase exhibited similar behavior for both catalyst precursors (Figure 5b,c).

3.2.2. Effect of the Feed Gas Composition. The feed gas composition in terms of the $O_2/H_2O/CH_3OH$ ratio was another important reaction variable that could strongly influence the catalytic activity. As shown in Figure 6, the increase of the H_2O/CH_3OH ratio from 1.3 to 4.0, under SRM conditions, led to a slight improvement of both the CH_3OH conversion and selectivity of CO_2 and H_2 between 250 and 425 °C. Above ~400 °C, a progressive drop of the CO_2 and H_2 selectivity with the temperature increase was observed for the H_2O/CH_3OH ratio of 1.3, which was associated with the RWGS effect. In contrast, the feed gas compositions with a larger excess of water exhibited a slight increase of both CO_2 and H_2. This behavior was related to the equilibrium of the WGS, which was thermodynamically predominant above 400 °C for high H_2O/CH_3OH ratios, thus contributing to the formation of CO_2 and H_2 at the expense of CO.

On the other hand, the effect of the H_2O/CH_3OH ratio was also significant to the stability of the catalyst. While no remarkable deactivation of the catalyst activity was observed using an H_2O/CH_3OH ratio of 4.0, a progressive activity loss with the time-on-stream reaction was detected for a ratio of 1.3. This was attributed to the carbon deposition because the carbon present in the catalyst was observed by SEM−EDS analysis. Therefore, the feed gas composition with the most water excess (H_2O/CH_3OH = 4.0) yielded better CH_3OH conversion and CO_2 and H_2 selectivity and stability in the whole temperature range than that close to the stoichiometric one (H_2O/CH_3OH = 1.3).

Finally, the effect of the addition of O_2 to SRM ($O_2/H_2O/CH_3OH$ = 0.1−0.3/1.3/1.0) on the catalytic performance was

https://doi.org/10.1021/acsaem.3c00778
ACS Appl. Energy Mater. 2023, 6, 7887−7898

studied. As shown in Figure 6, CH_3OH conversion under OSRM, compared to SRM, revealed a slight shift in the temperature at which the catalyst started to be active. This was attributed to the presence of O_2 because it could slightly deactivate the catalyst surface at low methanol conversions without H_2 and CO production. Then, the Co surface could be reoxidized to cobalt oxide, deactivating the catalyst for methanol reforming. At higher temperatures, the gas mixture becomes reductive again, and cobalt oxide is transformed into metallic Co because the combustion consumes O_2. As a consequence, CH_3OH conversion and product selectivity presented a similar trend in both processes. As expected, while H_2 generation decreased with the addition of O_2, CO_2 increased. For instance, for an initial molar ratio of $O_2/H_2O/CH_3OH$ = 0.2/1.3/1.0, the corresponding H_2O/CH_3OH ratio after complete O_2 consumption would be close to 2. Thus, OSRM was a way of increasing the H_2O/CH_3OH ratio and decreasing CO_2 production by hindering RWGS. In addition, no significant deactivation of the catalyst activity with the time-on-stream reaction was observed in OSRM. Therefore, the addition of O_2 to the SRM reaction could be an effective way of avoiding carbon deposition and increasing the CO_2 selectivity, consequently decreasing CO generation.

3.3. Catalyst Characterization after SRM and OSRM. In order to study the evolution of the phases formed at the catalyst under SRM and OSRM, all samples were characterized by using XRD. Figure 7 shows the XRD patterns of the as-prepared catalyst and after testing under SRM and OSRM conditions at 600 °C for 1 h and quenched in a N_2 atmosphere. After the SRM and OSRM reactions, the characteristic diffraction peaks of hexagonal La_2O_3, hexagonal $La(OH)_3$, monoclinic $La_2O_2CO_3$, cubic SrO, orthorhombic $SrCO_3$, cubic Co^0, and cubic CoO were detected, and no peaks of LSC were observed (Figure 7b,c). This evidenced that Co ions were reduced from the perovskite lattice to Co^0 nanoparticles, which were highly dispersed on a matrix of lanthanum and strontium oxides ($Co/La_2O_3/SrO$). The Co^0 crystallite sizes determined from the XRD data with Scherrer's formula were 20−30 nm. In addition, other species such as $La_2O_2CO_3$, $La(OH)_3$, $SrCO_3$, and CoO were also formed under the SRM and OSRM conditions. The reactions of La_2O_3 with H_2O and SrO with CO_2 as reaction products generated $La(OH)_3$ and $SrCO_3$ (eqs 5 and 6, respectively).

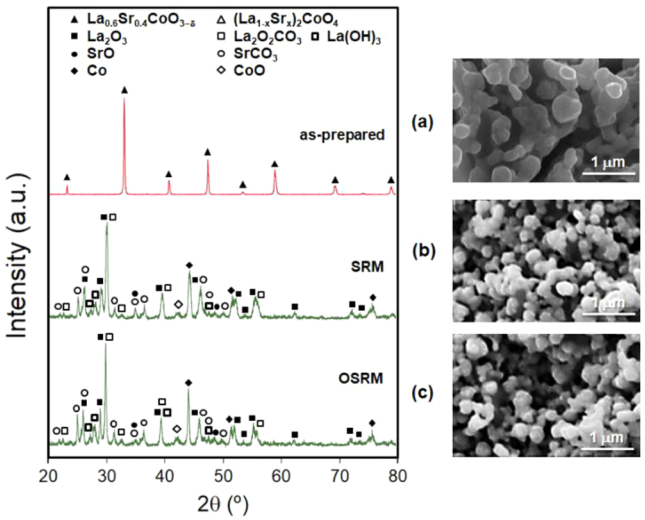

Figure 7. XRD patterns and SEM images for LSC: (a) as-prepared and after prereduction in 5% H_2/Ar at 600 °C for 1 h, operating under (b) SRM and (c) OSRM at 600 °C for 1 h, and quenching in a N_2 atmosphere. Phases identified from JCPDS cards were as follows: cubic $La_{0.6}Sr_{0.4}CoO_{3-\delta}$ (JCPDS 48-0121), hexagonal La_2O_3 (JCPDS 05-0602), hexagonal $La(OH)_3$ (JCPDS 36-1481), monoclinic $La_2O_2CO_3$ (JCPDS 48-1113), cubic SrO (JCPDS 48-1477), orthorhombic $SrCO_3$ (JCPDS 05-0418), cubic Co (JCPDS 15-0806), and cubic CoO (JCPDS 71-1178).

$$SrO + CO_2 \leftrightarrow SrCO_3 \quad (5)$$

$$La_2O_3 + 3H_2O \leftrightarrow 2La(OH)_3 \quad (6)$$

As reported in previous works,[62−64] the presence of $La_2O_2CO_3$ was especially interesting because lanthanum oxycarbonate species could react with surface carbon in their vicinity, thus cleaning the Co surface of the carbon deposits. In this way, the adsorbed CO_2 on La_2O_3 formed $La_2O_2CO_3$ (eq 7), which could react with neighboring active carbonaceous intermediate species to produce CO and regenerate La_2O_3, completing the cycle between $La_2O_2CO_3$ and La_2O_3 (eq 8):

$$La_2O_3 + CO_2 \leftrightarrow La_2O_2CO_3 \quad (7)$$

$$La_2O_2CO_3 + C \rightarrow La_2O_3 + 2CO \quad (8)$$

This mechanism described the good stability of the catalysts based on M/La_2O_3 (M = Co, Ni, etc.) under reforming reaction conditions because active metal particles were decorated with lanthanum oxide species originating from the support. Regeneration of the active sites took place in the vicinity of lanthanum oxide particles with an intermediate formation of $La_2O_2CO_3$. However, this mechanism in the LSC precursor showed limited efficiency in severe SRM conditions because catalyst deactivation was observed for nearly stoichiometric feed ratios (H_2O/CH_3OH = 1.3). Thus, the good catalyst stability exhibited under SRM for an H_2O/CH_3OH ratio of 4, and also under OSRM, could be attributed to the influence of lanthanum oxycarbonate. As shown in Figure 7, the formation of lanthanum oxycarbonate was favorable in a high excess of water and an addition of O_2, which reduced the potential catalyst deactivation caused by carbon deposition. SEM micrographs confirmed that both the dispersion and size of the particles after reduction of the catalyst precursor were more significant than those of the as-prepared ones (Figure 7). Similarly, the specific surface area of the as-prepared catalyst precursor (6 $m^2\ g^{-1}$) was strongly increased to 25 and 28 $m^2\ g^{-1}$ after testing and quenching in N_2 under SRM and OSRM, respectively. The superior catalytic performance of OSRM compared to SRM was attributed to the higher surface area, higher metal dispersion, and smaller size of the Co^0 nanoparticles.

3.4. Catalytic Performance in Redox Cyclic Tests. As mentioned above, the best resistance of the catalyst to deactivation due to carbon deposition was under OSRM reaction conditions ($O_2/H_2O/CH_3OH$ = 0.1−0.3/1.3/1.0). Therefore, these reaction conditions were selected to evaluate the effect of redox cycles on the catalytic activity and *in situ* self-regeneration of the catalyst, thus completely repeating several times the process of reduction and oxidation for the same sample. Figure 8 shows the CH_3OH conversion and selectivity of CO_2 and H_2 of the precursor focused on two different cyclic tests: (a) operating under OSRM at 600 °C for 1 h and slow cooling to RT under OSRM (Figure 8a) and (b)

https://doi.org/10.1021/acsaem.3c00778
ACS Appl. Energy Mater. 2023, 6, 7887−7898

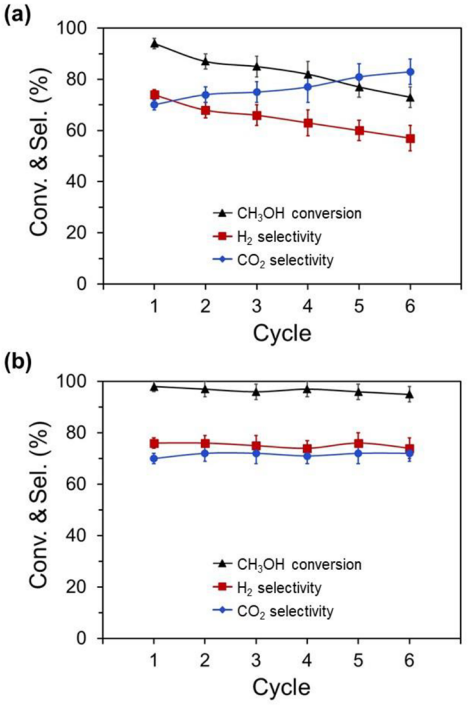

Figure 8. CH_3OH conversion and selectivity of H_2 and CO_2 in the redox cyclic tests operating under OSRM reaction conditions at 600 °C and $O_2/H_2O/CH_3OH$ = 0.1−0.3/1.3/1.0 and subsequently (a) slow cooling to RT under OSRM and (b) reoxidized in air at 900 °C and then slow cooling to RT in air.

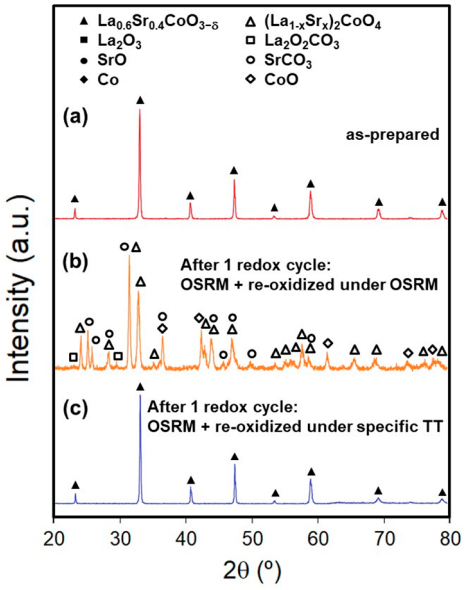

Figure 9. XRD patterns for LSC: (a) as-prepared; (b) after one redox cycle of prereducing in 5% H_2/Ar at 650 °C for 1 h, operating under OSRM at 600 °C for 1 h, and slow cooling to RT under OSRM; (c) after one redox cycle of prereducing in 5% H_2/Ar at 650 °C for 1 h, operating under OSRM at 600 °C for 1 h, and reoxidized under specific thermal treatment of regeneration in air at 900 °C for 12 h and in pure O_2 at 300 °C for 72 h. Phases identified from JCPDS cards were as follows: cubic $La_{0.6}Sr_{0.4}CoO_{3-\delta}$ (JCPDS 48-0121), tetragonal $(La_{1-x}Sr_x)_2CoO_4$ (x = 0; JCPDS 34-1296), monoclinic $La_2O_2CO_3$ (JCPDS 48-1113), orthorhombic $SrCO_3$ (JCPDS 05-0418), and cubic CoO (JCPDS 71-1178).

operating under OSRM and reoxidized in air at 900 °C and then slow cooling to RT in air (Figure 8b). In the redox cyclic tests under OSRM, both the CH_3OH conversion and H_2 selectivity were strongly decreased with an increase in the redox cycles. In contrast, the CH_3OH conversion and selectivity of CO_2 and H_2 during the six cyclic tests with a specific thermal treatment remained almost constant, indicating that the conditions of the reoxidation process play a remarkable role in the performance and stability of the catalyst in successive redox processes.

3.5. Catalyst Characterization after Redox Cyclic Tests. XRD analyses were carried out to determine the evolution of phases in the LSC precursor after redox cyclic tests under OSRM and *in situ* self-regeneration of the catalyst (Figure 9). As shown in Figure 9, the XRD patterns after the first cycle exhibited the formation of the tetragonal phase $[T'(La_{1-x}Sr_x)_2CoO_4]$ due to the reaction of La_2O_3, SrO, and Co favored by slow cooling during the cyclic tests. In addition, a small fraction of La, Sr, and Co remained as $La_2O_2CO_3$, $SrCO_3$, and CoO. Therefore, the self-regeneration process of the catalyst in a redox cycle was not completed under the OSRM reaction conditions. However, the XRD results evidenced that the used catalyst after one redox cycle could be regenerated entirely under a reoxidation thermal treatment in synthetic air at 900 °C for 12 h and finally in pure O_2 at 300 °C for 72 h (Figure 9c). Complete regeneration of the used catalyst suggests that Co nanoparticles were highly dispersed on the matrix of lanthanum and strontium carbonates and oxides under OSRM, which could be interesting for the mitigation of Co coarsening and the deactivation of the catalyst in operation. In another series of experiments, degradation and regeneration were studied in successive redox cycles (Figure 10). After six redox cycles, the XRD patterns showed higher amounts of the same compounds ($[T'(La_{1-x}Sr_x)_2CoO_4]$, $La_2O_2CO_3$, $SrCO_3$, and CoO) compared to the first cycle (Figure 10b,c). In this regard, the used catalyst after six redox cycles could not be regenerated entirely under a reoxidation thermal treatment in synthetic air at 900 °C for 12 h and finally in pure O_2 at 300 °C for 72 h (Figure 10d). In this case, the catalyst presented small amounts of $(La_{1-x}Sr_x)_2CoO_4$, and the presence of $SrCO_3$ and CoO was also detected; therefore, the irreversible segregation of Sr-rich species took place.

SEM images of the as-prepared catalyst and after redox cyclic tests and thermal treatment of regeneration are shown in Figure 11. After the first redox cycle, the used catalyst and slow cooling in OSRM presented slightly smaller particle sizes than the as-prepared and regenerated catalysts (Figure 11a,b,d). However, after the sixth cycle, it can be observed that both the used catalyst (slow cooling under OSRM) and the regenerated catalyst exhibited the grains bonded together slightly, evidencing a slight sintering after redox cycles at high temperature (Figure 11a,c,e). In addition, the morphology of the used catalysts after the first cycle (Figure 10b,d) exhibited more porosity and larger voids between particles compared to the six cycles (Figure 11c,e). The interconnected porosity and voids between the particles enable the diffusion of reactant and product gas into the solid particles. These observations in the microstructures are consistent with the values of the specific surface area because the used catalyst after the first cycle presented a higher specific surface area (12 $m^2\ g^{-1}$) than the regenerated catalyst (7 $m^2\ g^{-1}$) and the as-prepared one (6 $m^2\ g^{-1}$). In contrast, the specific surface area significantly decreased during successive redox cycles, reaching values of

https://doi.org/10.1021/acsaem.3c00778
ACS Appl. Energy Mater. 2023, 6, 7887−7898

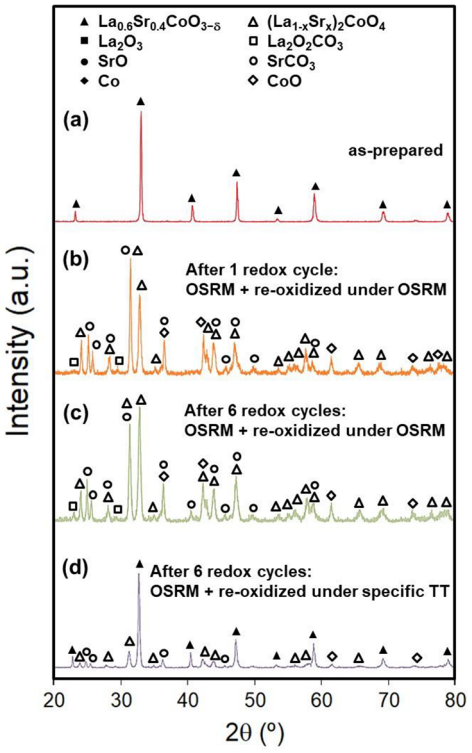

Figure 10. XRD patterns for LSC: (a) as-prepared; (b) after one redox cycle of prereducing in 5% H_2/Ar at 650 °C for 1 h, operating under OSRM at 600 °C for 1 h, and slow cooling to RT under OSRM; (c) after six redox cycles, repeating 6 times similar to one cycle, and slow cooling to RT under OSRM; (d) after six cycles and regeneration in air at 900 °C for 12 h and in pure O_2 at 300 °C for 72 h. Phases identified from JCPDS cards were as follows: cubic $La_{0.6}Sr_{0.4}CoO_{3-\delta}$ (JCPDS 48-0121), tetragonal $(La_{1-x}Sr_x)_2CoO_4$ (x = 0; JCPDS 34-1296), monoclinic $La_2O_2CO_3$ (JCPDS 48-1113), orthorhombic $SrCO_3$ (JCPDS 05-0418), and cubic CoO (JCPDS 71-1178).

8 and 5 $m^2\ g^{-1}$ (after six cycles) for the slow cooling and regenerated catalysts, respectively.

With the experimental observations discussed above, we can suggest how the different programs of the redox cycles (in terms of reoxidation and cooling from the operation temperature to RT) affect the regeneration of a catalyst. In the first program of the redox cycle, reoxidation of the catalyst with slow cooling under OSRM caused severe degradation of the catalytic activity in successive redox cycles. This was attributed to a remarkable segregation of phases [$(La_{1-x}Sr_x)_2CoO_4$, $SrCO_3$, ...] with the accumulation of redox cycles in an irreversible way, of which the entire regeneration of the catalyst using a regeneration thermal treatment is difficult. As reported in previous studies of LSC for electrochemical applications such as SOFCs,[46,65] the accumulation of Sr-rich species, particularly $SrCO_3$, on the catalyst surface covered the catalytically active Co surface sites, thus very effectively decreasing the catalytic activity of LSC. In the second program of the redox cycle, the use of a specific regeneration treatment in air at 900 °C between consecutive cycles stopped degradation of the catalytic activity, which suggests that the regenerated LSC presented a surface quite similar to the original one.

4. CONCLUSIONS

SRM and OSRM over LSC perovskite, as a catalyst precursor, were studied to supply syngas enriched in H_2 for SOFC applications. The SRM performance of the catalyst precursor strongly depended on the initial oxidation state of the catalyst, feed gas composition, and reaction temperature. CH_3OH conversion of the catalyst with a reductive pretreatment at 650 °C was significantly enhanced at lower temperatures than the as-prepared one. Sr doping in $LaCoO_3$-based perovskites facilitated the reduction process for the as-prepared catalyst precursor. Consequently, CH_3OH conversion of LSC under SRM was increased at lower temperatures compared to undoped $LaCoO_3$. MD and RWGS occurred simultaneously with SRM and OSRM. The SRM performance was also significantly affected by the feed gas composition. The feed composition with significant water excess (CH_3OH/H_2O = 4.0) yielded better CO_2 and H_2 selectivity (at temperatures of >400 °C) than that close to the stoichiometric one due to the increases of the WGS reaction. In addition, this reduced the potential catalyst deactivation caused by carbon deposition. In OSRM, adding O_2 to SRM was an effective way of avoiding carbon deposition but at the expense of reducing the H_2 selectivity and increasing the CO_2 selectivity. The character-

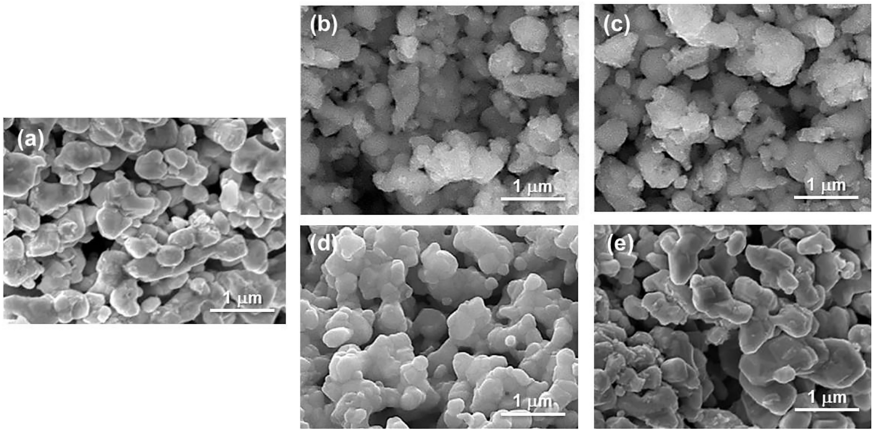

Figure 11. SEM images of LSC: (a) as-prepared; after (b) one and (c) six redox cycles, operating under OSRM at 600 °C for 1 h and slow cooling to RT under OSRM; after (d) one and (e) six redox cycles, operating under OSRM at 600 °C for 1 h and a regeneration thermal treatment in air at 900 °C for 12 h and in pure O_2 at 300 °C for 72 h.

https://doi.org/10.1021/acsaem.3c00778
ACS Appl. Energy Mater. 2023, 6, 7887−7898

ization results evidenced the stability of highly dispersed Co nanoparticles over a matrix composed of metal carbonates and oxides, mainly La_2O_3, $La_2O_2CO_3$, SrO, and $SrCO_3$. In addition, the formation of lanthanum oxycarbonate could also contribute to minimizing carbon deposition on the catalyst surface.

The identification of O loss and certain segregation of Sr-rich species on the reduced precursor surface by XPS evidenced a strong connection between the surface chemistry and catalytic activity. The reoxidation program in repetitive redox cycles played a crucial role in the regeneration of catalysts. A reoxidation with slow cooling under OSRM contributed to a severe degradation of the catalytic activity in successive redox cycles probably due to the accumulation of Sr-rich species ($SrCO_3$) on the catalyst surface, thus covering the catalytically active Co surface sites. In contrast, the reoxidized catalyst in air at 900 °C and then slow cooling to RT between consecutive redox cycles stopped degradation of the catalytic activity. Furthermore, the catalyst precursor could be regenerated to the initial perovskite structure with a specific regeneration treatment (in air at 900 °C for 12 h and in pure O_2 at 300 °C for 72 h). The authors recognize that these results do not demonstrate long-term cycling stability of LSC; however, it can be an effective approach to mitigating the degradation of LSC, enabling its practical application in catalysis but also in other systems such as SOECs for renewable energy conversion and storage.

AUTHOR INFORMATION

Corresponding Author

Miguel Morales − *CIEFMA—Department of Materials Science and Engineering, EEBE—Campus Diagonal Besòs, Universitat Politècnica de Catalunya—BarcelonaTech, 08019 Barcelona, Spain; Barcelona Research Center in Multiscale Science and Engineering, Universitat Politècnica de Catalunya—BarcelonaTech, 08019 Barcelona, Spain;* orcid.org/0000-0003-0702-1966; Email: miguel.morales-comas@upc.edu

Authors

Miguel Ángel Laguna-Bercero − *Instituto de Nanociencia y Materiales de Aragón, INMA, CSIC, Universidad de Zaragoza, 50009 Zaragoza, Spain;* orcid.org/0000-0002-7819-8956

Emilio Jiménez-Piqué − *CIEFMA—Department of Materials Science and Engineering, EEBE—Campus Diagonal Besòs, Universitat Politècnica de Catalunya—BarcelonaTech, 08019 Barcelona, Spain; Barcelona Research Center in Multiscale Science and Engineering, Universitat Politècnica de Catalunya—BarcelonaTech, 08019 Barcelona, Spain;* orcid.org/0000-0002-6950-611X

Complete contact information is available at: https://pubs.acs.org/10.1021/acsaem.3c00778

Notes

The authors declare no competing financial interest.

ACKNOWLEDGMENTS

This research has been supported by Grants PID2021-126614OB-I00 and PID2019-107106RB-C32, funded by MCIN/AEI/10.13039/501100011033 and FEDER. Additional funding has been received from AGAUR, Agency for Administration of University and Research (2021 SGR 01053). M.M. is a Serra Húnter Lecturer Professor, and he is grateful to the Serra Húnter program (Generalitat de Catalunya).

REFERENCES

(1) Larminie, J.; Dicks, A. Fuel Cell Systems Explained Second Edition. https://www.bcsd.org/site/handlers/filedownload.ashx?moduleinstanceid=1973&dataid=9790&FileName=fuel%20cell%20pdf.pdf.

(2) Iulianelli, A.; Ribeirinha, P.; Mendes, A.; Basile, A. Methanol Steam Reforming for Hydrogen Generation via Conventional and Membrane Reactors: A Review. *Renew. Sustain. Energy Rev.* **2014**, *29*, 355−368.

(3) Herdem, M. S.; Sinaki, M. Y.; Farhad, S.; Hamdullahpur, F. An Overview of the Methanol Reforming Process: Comparison of Fuels, Catalysts, Reformers, and Systems. *Int. J. Energy Res.* **2019**, *43*, 5076−5105.

(4) Schorn, F.; Peters, R.; Stolten, D.; Schnorbus, T.; Heuser, B.; Breuer, J. L.; Samsun, R. C. Methanol as a Renewable Energy Carrier: An Assessment of Production and Transportation Costs for Selected Global Locations. *Adv. Appl. energy* **2021**, *3*, 100050.

(5) Bos, M. J.; Kersten, S. R. A.; Brilman, D. W. F. Wind Power to Methanol: Renewable Methanol Production Using Electricity, Electrolysis of Water and CO_2 Air Capture. *Appl. Energy* **2020**, *264*, 114672.

(6) Shi, C.; Labbaf, B.; Mostafavi, E.; Mahinpey, N. Methanol Production from Water Electrolysis and Tri-Reforming: Process Design and Technical-Economic Analysis. *J. CO2 Util.* **2020**, *38*, 241−251.

(7) Tosti, S.; Basile, A.; Borgognoni, F.; Capaldo, V.; Cordiner, S.; Di Cave, S.; Gallucci, F.; Rizzello, C.; Santucci, A.; Traversa, E. Low Temperature Ethanol Steam Reforming in a Pd-Ag Membrane Reactor. Part 1: Ru-Based Catalyst. *J. Membr. Sci.* **2008**, *308*, 250−257.

(8) Ogo, S.; Sekine, Y. Recent Progress in Ethanol Steam Reforming Using Non-Noble Transition Metal Catalysts: A Review. *Fuel Process. Technol.* **2020**, *199*, 106238.

(9) Chen, Y.; Wang, Y.; Xu, H.; Xiong, G. Hydrogen Production Capacity of Membrane Reformer for Methane Steam Reforming near Practical Working Conditions. *J. Membr. Sci.* **2008**, *322*, 453−459.

(10) Peppley, B. A.; Amphlett, J. C.; Kearns, L. M.; Mann, R. F. Methanol-Steam Reforming on $Cu/ZnO/Al_2O_3$. Part 1: The Reaction Network. *Appl. Catal. A Gen.* **1999**, *179*, 21−29.

(11) Peppley, B. A.; Amphlett, J. C.; Kearns, L. M.; Mann, R. F. Methanol-Steam Reforming on Cu/ZnO/Al2O3 Catalysts. Part 2. A Comprehensive Kinetic Model. *Appl. Catal. A Gen.* **1999**, *179*, 31−49.

(12) Mosińska, M.; Szynkowska-Jóźwik, M. I.; Mierczyński, P. Catalysts for Hydrogen Generation via Oxy-Steam Reforming of Methanol Process. *Mater. (Basel, Switzerland)* **2020**, *13*, 5601.

(13) Sá, S.; Silva, H.; Brandão, L.; Sousa, J. M.; Mendes, A. Catalysts for Methanol Steam Reforming—A Review. *Appl. Catal. B Environ.* **2010**, *99*, 43−57.

(14) Halevi, B.; Peterson, E. J.; Roy, A.; Delariva, A.; Jeroro, E.; Gao, F.; Wang, Y.; Vohs, J. M.; Kiefer, B.; Kunkes, E.; et al. Catalytic Reactivity of Face Centered Cubic PdZn α for the Steam Reforming of Methanol. *J. Catal.* **2012**, *291*, 44−54.

(15) Xu, X.; Shuai, K.; Xu, B. Review on Copper and Palladium Based Catalysts for Methanol Steam Reforming to Produce Hydrogen. *Catalysts* **2017**, *7*, 183.

(16) Purnama, H.; Ressler, T.; Jentoft, R. E.; Soerijanto, H.; Schlögl, R.; Schomäcker, R. CO Formation/Selectivity for Steam Reforming of Methanol with a Commercial CuO/ZnO/Al2O3 Catalyst. *Appl. Catal. A Gen.* **2004**, *259*, 83−94.

(17) Royer, S.; Duprez, D.; Can, F.; Courtois, X.; Batiot-Dupeyrat, C.; Laassiri, S.; Alamdari, H. Perovskites as Substitutes of Noble Metals for Heterogeneous Catalysis: Dream or Reality. *Chem. Rev.* **2014**, *114*, 10292−10368.

(18) Yang, Q.; Liu, G.; Liu, Y. Perovskite-Type Oxides as the Catalyst Precursors for Preparing Supported Metallic Nanocatalysts: A Review. *Ind. Eng. Chem. Res.* **2018**, *57*, 1−17.
(19) Glisenti, A.; Galenda, A.; Natile, M. M. Steam Reforming and Oxidative Steam Reforming of Methanol and Ethanol: The Behaviour of $LaCo_{0.7}Cu_{0.3}O_3$. *Appl. Catal. A Gen.* **2013**, *453*, 102−112.
(20) Kuc, J.; Weidenkaff, A.; Matam, K. Methanol Steam Reforming on Perovskite-Type Oxides $LaCo_{1-x-y}Pd_xZn_yO_{3\pm\delta}$: Effect of Pd/Zn on CO_2 Selectivity. *Top. Catal.* **2015**, *58* (14), 905−907.
(21) Kuc, J.; Neumann, M.; Armbrüster, M.; Yoon, S.; Zhang, Y.; Erni, R.; Weidenkaff, A.; Matam, S. K. Methanol Steam Reforming Catalysts Derived by Reduction of Perovskite-Type Oxides $LaCo_{1-x-y}Pd_xZn_yO_{3\pm\delta}$. *Catal. Sci. Technol.* **2016**, *6*, 1455−1468.
(22) Zhang, Y.; Zhao, Y.; Hao, Y. A Study on Steam Reforming of Methanol over a Novel Nanocatalyst of Compound Metal Oxides. *Energy Procedia* **2018**, *152*, 192−197.
(23) Qiao, W. J.; Xiao, G. P.; Zhang, L.; Qing, S. J.; Zhao, Y. Q.; Geng, Z. X.; Gao, Z. X. Catalytic Performance of $CuO/La_{1-x}Ce_xCrO_3$ in the Steam Reforming of Methanol. *Ranliao Huaxue Xuebao/Journal Fuel Chem. Technol.* **2021**, *49*, 205−210.
(24) Shao, Z.; Shen, Q.; Ding, H.; Jiang, Y.; Li, S.; Yang, G. Synthesis, Characterization, and Methanol Steam Reforming Performance for Hydrogen Production on Perovskite-Type Oxides $SrCo_{1-X}Cu_xO_{3-\delta}$. *Ceram. Int.* **2022**, *48* (8), 11836−11848.
(25) Costa, P.; Pinto, F.; André, R. N.; Marques, P. Integration of Gasification and Solid Oxide Fuel Cells (SOFCs) for Combined Heat and Power (CHP). *Process. 2021, Vol. 9, Page 254* **2021**, *9*, 254.
(26) Natile, M. M.; Poletto, F.; Galenda, A.; Glisenti, A.; Montini, T.; De Rogatis, L.; Fornasiero, P. $La_{0.6}Sr_{0.4}Co_{1-y}Fe_yO_{3-\delta}$ Perovskites: Influence of the Co/Fe Atomic Ratio on Properties and Catalytic Activity toward Alcohol Steam-Reforming. *Chem. Mater.* **2008**, *20* (6), 2314−2327.
(27) Ma, F.; Ding, Z.; Chu, W.; Hao, S.; Qi, T. Preparation of La_XCoO_3 (X = Mg, Ca, Sr, Ce) Catalysts and Their Performance for Steam Reforming of Ethanol to Hydrogen. *Chin. J. Catal.* **2014**, *35*, 1768−1774.
(28) Nakamura, T.; Misono, M.; Yoneda, Y. Reduction-Oxidation and Catalytic Properties of La1 - XSrxCoO3. *J. Catal.* **1983**, *83*, 151−159.
(29) Tabata, K.; Kohiki, S. Effects of Thermal Treatment on the Catalytic Properties of $LaCoO_3$ and $La_{0.8}Sr_{0.2}CoO_{3-\delta}$. *J. Mater. Sci.* **1988**, *23*, 1056−1059.
(30) Prasad, D. H.; Park, S. Y.; Oh, E. O.; Ji, H.; Kim, H. R.; Yoon, K. J.; Son, J. W.; Lee, J. H. Synthesis of Nano-Crystalline $La_{1-X}Sr_xCoO_{3-\delta}$ Perovskite Oxides by EDTA-Citrate Complexing Process and Its Catalytic Activity for Soot Oxidation. *Appl. Catal. A Gen.* **2012**, *447−448*, 100−106.
(31) Li, X.; Dai, H.; Deng, J.; Liu, Y.; Zhao, Z.; Wang, Y.; Yang, H.; Au, C. T. In Situ PMMA-Templating Preparation and Excellent Catalytic Performance of Co_3O_4/3DOM La0.6Sr0.4CoO3 for Toluene Combustion. *Appl. Catal. A Gen.* **2013**, *458*, 11−20.
(32) Sun, N.; Liu, H.; Yu, Z.; Zheng, Z.; Shao, C. The $La_{0.6}Sr_{0.4}CoO_3$ Perovskite Catalyst for Li-O_2 Battery. *Solid State Ionics* **2014**, *268*, 125−130.
(33) García-López, E.; Marcì, G.; Puleo, F.; La Parola, V.; Liotta, L. F. $La_{1-x}Sr_xCo_{1-y}Fe_yO_{3-\delta}$ Perovskites: Preparation, Characterization and Solar Photocatalytic Activity. *Appl. Catal. B Environ.* **2015**, *178*, 218−225.
(34) Tsipis, E. V.; Kharton, V. V. Electrode Materials and Reaction Mechanisms in Solid Oxide Fuel Cells: A Brief Review. *J. Solid State Electrochem. 2008 1211* **2008**, *12*, 1367−1391.
(35) Nechache, A.; Cassir, M.; Ringuedé, A. Solid Oxide Electrolysis Cell Analysis by Means of Electrochemical Impedance Spectroscopy: A Review. *J. Power Sources* **2014**, *258*, 164−181.
(36) Morales, M.; Laguna-Bercero, M. A.; Jiménez-Piqué, E. Direct-Methane Anode-Supported Solid Oxide Fuel Cells Fabricated by Aqueous Gel-Casting. *J. Eur. Ceram. Soc.* **2023**, *43*, 2740−2751.
(37) Laguna-Bercero, M. A. Recent Advances in High Temperature Electrolysis Using Solid Oxide Fuel Cells: A Review. *J. Power Sources* **2012**, *203*, 4−16.
(38) Pandiyan, A.; Uthayakumar, A.; Subrayan, R.; Cha, S. W.; Krishna Moorthy, S. B. Review of Solid Oxide Electrolysis Cells: A Clean Energy Strategy for Hydrogen Generation. *https://doi.org/10.1680/jnaen.18.00009* **2019**, *8*, 2−22.
(39) Bernadet, L.; Morales, M.; Capdevila, X. G.; Ramos, F.; Monterde, M. C.; Calero, J. A.; Morata, A.; Torrell, M.; Tarancón, A. Reversible Fuel Electrode Supported Solid Oxide Cells Fabricated by Aqueous Multilayered Tape Casting. *J. Phys. Energy* **2021**, *3*, 024002.
(40) Morales, M.; Roa, J. J.; Tartaj, J.; Segarra, M. Performance and Short-Term Stability of Single-Chamber Solid Oxide Fuel Cells Based on $La_{0.9}Sr_{0.1}Ga_{0.8}Mg_{0.2}O_{3-\delta}$ Electrolyte. *J. Power Sources* **2012**, *216*, 417.
(41) Morales, M.; Espiell, F.; Segarra, M. Improvement of Performance in Low Temperature Solid Oxide Fuel Cells Operated on Ethanol and Air Mixtures Using Cu-ZnO-Al_2O_3 catalyst Layer. *J. Power Sources* **2015**, *293*, 366.
(42) Piñol, S.; Morales, M.; Espiell, F. Hydrogen Production by a New Selective Partial Oxidation of Methane in Air Using Reducted $La_{0.5}Sr_{0.5}CoO_{3-\delta}$ as Catalyst for Fuel Cell Applications. *J. New Mater. Electrochem. Syst.* **2008**, *11*.
(43) Morales, M.; Espiell, F.; Segarra, M. Performance and Stability of $La_{0.5}Sr_{0.5}CoO_{3-\delta}$ Perovskite as Catalyst Precursor for Syngas Production by Partial Oxidation of Methane. *Int. J. Hydrogen Energy* **2014**, *39*, 6454.
(44) Morales, M.; Segarra, M. Steam Reforming and Oxidative Steam Reforming of Ethanol over $La_{0.6}Sr_{0.4}CoO_{3-\delta}$ Perovskite as Catalyst Precursor for Hydrogen Production. *Appl. Catal. A Gen.* **2015**, *502*, 305.
(45) Chen, G.; Shen, Q.; Zhang, X.; Cai, Z.; Shao, Z.; Li, S.; Yang, G. Methanol Steam Reforming over $La_{1-X}Sr_xCeO_{3-\delta}$ Catalysts for Hydrogen Production: Optimization of Operating Parameters. *Catal. 2023, Vol. 13, Page 248* **2023**, *13*, 248.
(46) Koo, B.; Kim, K.; Kim, J. K.; Kwon, H.; Han, J. W.; Jung, W. C. Sr Segregation in Perovskite Oxides: Why It Happens and How It Exists. *Joule* **2018**, *2*, 1476−1499.
(47) Yang, J.; Chen, L.; Cai, D.; Zhang, H.; Wang, J.; Guan, W. Study on the Strontium Segregation Behavior of Lanthanum Strontium Cobalt Ferrite Electrode under Compression. *Int. J. Hydrogen Energy* **2021**, *46*, 9730−9740.
(48) Chen, K.; Jiang, S. P. Surface Segregation in Solid Oxide Cell Oxygen Electrodes: Phenomena, Mitigation Strategies and Electrochemical Properties. *Electrochem. Energy Rev.* **2020**, *3*, 730−765.
(49) Sha, Z.; Shen, Z.; Calì, E.; Kilner, J. A.; Skinner, S. J. Understanding Surface Chemical Processes in Perovskite Oxide Electrodes. *J. Mater. Chem. A* **2023**, *11*, 5645−5659.
(50) Siebenhofer, M.; Haselmann, U.; Nenning, A.; Friedbacher, G.; Ewald Bumberger, A. E.; Wurster, S.; Artner, W.; Hutter, H.; Zhang, Z.; Fleig, J.; Kubicek, M.; et al. Surface Chemistry and Degradation Processes of Dense $La_{0.6}Sr_{0.4}CoO_{3-\delta}$ Thin Film Electrodes. *J. Electrochem. Soc.* **2023**, *170*, 014501.
(51) Klug, H.; Alexander, L. *X-Ray Diffraction Procedures: For Polycrystalline and Amorphous Materials*, 2nd ed.; Wiley, New York, 1974; p 992.
(52) Fang, D.; He, F.; Xie, J.; Xue, L. Calibration of Binding Energy Positions with C1s for XPS Results. *J. Wuhan Univ. Technol. Mater. Sci. Ed.* **2020**, *35*, 711−718.
(53) Cheng, X.; Fabbri, E.; Nachtegaal, M.; Castelli, I. E.; El Kazzi, M.; Haumont, R.; Marzari, N.; Schmidt, T. J. Oxygen Evolution Reaction on $La_{1-X}Sr_xCoO_3$ Perovskites: A Combined Experimental and Theoretical Study of Their Structural, Electronic, and Electrochemical Properties. *Chem. Mater.* **2015**, *27*, 7662−7672.
(54) Qiang, J.; Wang, D.; Hui, S. Synthesis of $La_{1-X}Sr_xCoO_{3-\delta}$ and Its REDOX Performance in Air. *J. Environ. Chem. Eng.* **2022**, *10*, 108794.
(55) Zhu, J.; Li, H.; Zhong, L.; Xiao, P.; Xu, X.; Yang, X.; Zhao, Z.; Li, J. Perovskite Oxides: Preparation, Characterizations, and

Applications in Heterogeneous Catalysis. *ACS Catal.* **2014**, *4*, 2917−2940.
(56) Van Der Heide, P. A. W. Systematic X-Ray Photoelectron Spectroscopic Study of $La_{1-x}Sr_x$-Based Perovskite-Type Oxides. *Surf. Interface Anal.* **2002**, *33*, 414−425.
(57) Cunha, A. F.; Órfão, J. J. M.; Figueiredo, J. L. Catalytic Decomposition of Methane on Raney-Type Catalysts. *Appl. Catal. A Gen.* **2008**, *348*, 103−112.
(58) Wang, Z.; Wang, H.; Liu, Y. $La_{1-X}Ca_xFe_{1-X}Co_xO_3$ - A Stable Catalyst for Oxidative Steam Reforming of Ethanol to Produce Hydrogen. *RSC Adv.* **2013**, *3*, 10027−10036.
(59) Cai, Z.; Kubicek, M.; Fleig, J.; Yildiz, B. Chemical Heterogeneities on $La_{0.6}Sr_{0.4}CoO_{3-\delta}$ Thin Films-Correlations to Cathode Surface Activity and Stability. *Chem. Mater.* **2012**, *24*, 1116−1127.
(60) Dupin, J. C.; Gonbeau, D.; Vinatier, P.; Levasseur, A. Systematic XPS Studies of Metal Oxides, Hydroxides and Peroxides. *Phys. Chem. Chem. Phys.* **2000**, *2*, 1319−1324.
(61) Druce, J.; Ishihara, T.; Kilner, J. Surface Composition of Perovskite-Type Materials Studied by Low Energy Ion Scattering (LEIS). *Solid State Ionics* **2014**, *262*, 893−896.
(62) Fatsikostas, A. N.; Kondarides, D. I.; Verykios, X. E. Production of Hydrogen for Fuel Cells by Reformation of Biomass-Derived Ethanol. *Catal. Today* **2002**, *75*, 145−155.
(63) Chiou, J. Y. Z.; Lee, C. L.; Ho, K. F.; Huang, H. H.; Yu, S. W.; Wang, C. Bin Catalytic Performance of Pt-Promoted Cobalt-Based Catalysts for the Steam Reforming of Ethanol. *Int. J. Hydrogen Energy* **2014**, *39*, 5653−5662.
(64) Charisiou, N.; Tzounis, L.; Sebastian, V.; Hinder, S.; Baker, M.; Polychronopoulou, K.; Goula, M. Investigating the Correlation between Deactivation and the Carbon Deposited on the Surface of Ni/Al_2O_3 and Ni/La_2O_3-Al_2O_3 Catalysts during the Biogas Reform-Ing Reaction. *Appl. Surf. Sci.* **2019**, *474*, 42.
(65) Opitz, A. K.; Rameshan, C.; Kubicek, M.; Rupp, G. M.; Nenning, A.; Götsch, T.; Blume, R.; Hävecker, M.; Knop-Gericke, A.; Rupprechter, G.; Klotzer, B.; Fleig, J.; et al. The Chemical Evolution of the $La_{0.6}Sr_{0.4}CoO_{3-\delta}$ Surface Under SOFC Operating Conditions and Its Implications for Electrochemical Oxygen Exchange Activity. *Top. Catal.* **2018**, *61*, 2129−2141.

https://doi.org/10.1021/acsaem.3c00778
ACS Appl. Energy Mater. 2023, 6, 7887−7898